Highlighting research on generative AI enhanced battery development from Dr. Roland Brunner's group at Materials Center Leoben, Styria, Austria.
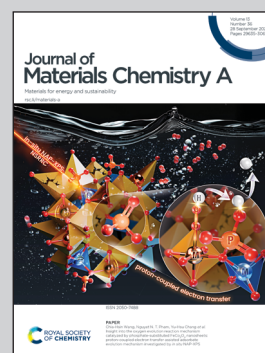
GenAI-enhanced 4D nano-tomography for advanced battery microstructure analysis

We demonstrate a generative AI-based workflow using the Inversion by Direct Iteration (InDI) algorithm to enhance 4D synchrotron X-ray nano-tomography of lithium-ion battery cells, doubling spatial resolution while preserving a large field-of-view and reducing photon density. This enables advanced high-fidelity visualization and quantification of dynamic microstructural changes during cycling of the battery cell. Ultimately, this workflow is not limited to X-ray nano-tomography but has potentially broad applicability across materials as well as medical imaging.

Image reproduced by permission of Raphael Wilhelmer, Michael Häusler and Roland Brunner from *J. Mater. Chem. A*, 2025, **13**, 29930.

Image created with Adobe Firefly.

As featured in:

See Roland Brunner *et al.*,
J. Mater. Chem. A, 2025, **13**, 29930.

ROYAL SOCIETY OF CHEMISTRY

ROYAL SOCIETY
OF CHEMISTRY

PAPER

Check for updates

GenAI-enhanced 4D nano-tomography for advanced battery microstructure analysis†

Michael Häusler, (ID) ‡[a] Raphael Wilhelmer, (ID) ‡[a] Rahulkumar J. Sinojiya,[a] Olga Stamati,[b] Julie Villanova,[c] Christoph Stangl,[d] Stefan Koller[d] and Roland Brunner (ID) *[a]

Monitoring the evolution of electrode microstructures at the sub-micron scale during electrochemical charging is crucial for elucidating battery aging mechanisms. Four-dimensional (4D) synchrotron X-ray nano-tomography (SXCT), defined as time-resolved three-dimensional (3D) imaging, allows the perception of such dynamic processes. Yet, 4D SXCT faces a dilemma between resolution and field-of-view including the troublesome invasive beam exposure. In this work, we demonstrate the potential of generative AI (genAI) models to significantly enhance 4D SXCT image datasets. Specifically, we apply a trained Inversion by Direct Iteration (InDI) algorithm suitable to improve the spatial resolution of measured unseen 4D SXCT image data, obtained during a lithiation cycle, by a factor of about two, while achieving an eight times larger field-of-view (FOV) as typically provided by such a resolution. Compared to other image enhancement algorithms like CNNs or GANs, InDI exhibits improved contrast and training stability. Besides, when compared to classical diffusion models, the number of iterations is reduced from several hundreds to roughly one dozen. Our results demonstrate the tremendous potential of the InDI model, facilitating enhanced possibilities to quantify the microstructure evolution during cycling with sufficient FOV and spatial resolution. Furthermore, the InDI framework has the potential to generalize as well as illustrate a broad applicability across many areas of materials science and imaging-driven fields, enabling the observation of dynamic processes on the nano-scale.

Introduction

Batteries play a vital role in enabling transport electrification and renewable energy storage, driving the transition towards a more sustainable energy landscape.[1,2] The growing demand for higher capacities, longer lifespans and improved safety necessitates the development of advanced battery materials and designs. The performance of a battery, whether in terms of capacity, energy density, or cycle life, is fundamentally governed by the intrinsic properties and dynamic behaviour of its constituent materials. Gaining a deeper understanding of these properties and their evolution during operation is crucial for the development of next-generation battery technologies.[1–4]

Silicon-based anodes are among the most promising candidates for next-generation lithium-ion batteries due to their exceptionally high theoretical capacity, approximately ten times that of conventional graphite anodes.[5–14] Consequently, they

have gained significant attention in the scientific community and are considered crucial for advanced energy storage solutions.[12] However, practical applications of silicon (Si) anodes face substantial challenges, particularly at high Si content, which is essential to reach higher energy densities and to meet the requirements for future e-mobility and storage applications.[6,11] During lithiation/delithiation, silicon undergoes large volume expansions and contractions, leading to particle fracture, pore formation, solid-electrolyte interphase (SEI) reformation and mechanical stress accumulation.[8,10,13] These underlying aging mechanisms cause microstructure degradation and are correlated with rapid capacity fade and limit the cycle life.[8,14] Understanding these dynamic processes, especially at the particle level is essential for overcoming these limitations and unlocking the full potential of silicon-based anodes.

Various high-resolution imaging techniques have been developed to study the microstructure of battery electrodes, including Si-particles, critical interfaces and material phases relevant to modern batteries.[15–25] Image quality plays a crucial role in enabling the extraction of physical descriptors through image classification, such as microstructural features, which are essential for modelling, process optimization, and materials development.

To date, researchers have predominantly relied on post-mortem investigations using high-resolution techniques such

[a]*Materials Center Leoben Forschung GmbH, 8700 Leoben, Austria. E-mail: roland.brunner@mcl.at*

[b]*Univ. Grenoble Alpes, CNRS, Grenoble INP, 3SR, 38000 Grenoble, France*

[c]*ESRF-The European Synchrotron, ID16B, 38000 Grenoble, France*

[d]*Varta Innovation GmbH, 8020 Graz, Austria*

‡ These authors contributed equally to this work.

as scanning electron microscopy (SEM) or transmission electron microscopy (TEM), as these methods are experimentally straightforward and widely accessible.[19,21,26] These methods feature high contrast and resolution, revealing particle shapes, particle interfaces and material phase information, as well as structural changes upon electrochemical loading conditions at the micro- and nanoscale.[26–29] These *ex situ* techniques are typically conducted under high vacuum conditions and often require invasive sample preparation steps that can alter the material's native state. While *in situ* variants, enabling us to witness the microstructure evolution over time, of SEM and TEM exist, they are limited by small sample volumes and idealized conditions, limiting their suitability for studying operational battery systems.[26,30,31]

X-ray-based methods, such as synchrotron X-ray computed tomography (SXCT), have emerged as powerful tools for three-dimensional imaging in battery research.[17,22–25] Their non-destructive nature allows repeated imaging of the same sample, allowing both post-mortem (*ex situ*) analyses of battery structures and *in situ* studies of structural evolution during operation.[23,32,33] Micro-SXCT, with voxel sizes in hundreds of nanometres, facilitates *ex* situ and *in situ* investigations of entire battery cells, including phenomena such as electrode cracking[34] and thermal effects.[35] However, its limited spatial resolution prevents the visualization of particle-level features, making it unsuitable for studying associated degradation mechanisms. Nano-SXCT addresses this limitation by offering a spatial resolution in the nm-regime, enabling high-resolution imaging at the level of individual electrodes.[22–24,33]

However, the benefits of nano-SXCT come with inherent trade-offs. High-resolution scans are typically restricted to small measurement volumes, ranging from a few micrometres to several hundred micrometres, which may not be representative of the overall electrode architecture.[22,24,33] While *in situ* nano-tomography has successfully been used to visualize micrometre-scale features such as crack propagation, pore formation and lithiation-induced structural changes at the electrode level, achieving sufficient signal-to-noise ratios under *in situ* conditions presents additional challenges.[23,24] Specifically, a high photon flux is often required to minimize motion artefacts during rapid scanning, which in turn increases the risk of beam-induced damage in sensitive battery materials.[36,37] Balancing the spatial resolution, field-of-view (FOV) and beam exposure remains a fundamental challenge for resolving sub-micrometre features across representative volumes.[17,33,38]

The enhancement and restoration of image quality is a fundamental problem in digital image processing, with broad applications ranging from medical imaging[39,40] and remote sensing[41,42] to digital photography and scientific visualization.[20,43] Techniques such as convolutional neural networks (CNNs),[44,45] generative adversarial networks (GANs),[44,46] and diffusion-based models[47,48] have shown the ability to recover intricate details, mostly outperforming classical algorithms such as histogram-equalization,[49,50] interpolation-algorithms[51] or denoising filters.[39,52] Nevertheless, CNNs are affected by regression-to-the-mean,[53,54] GANs suffer from training instability[46] and diffusion models, while offering stable training and

high-quality outputs, are computationally expensive due to their iterative nature. Additionally, diffusion models require an analytic form of the degradation process as prior knowledge.[54]

A promising alternative to the aforementioned methods is the recently introduced diffusion-like Inversion by Direct Iteration (InDI) algorithm for realistic and detailed image restoration.[54] Unlike conventional generative diffusion models[55] which start with an image typically consisting of purely Gaussian noise, InDI uses a pair of low-quality/high-quality (LQ/HQ) images, starting with the low-quality image as an input and refining it iteratively in several steps by learning the physical degradation processes. Using the LQ image as prior also significantly reduces the number of iterations and simplifies the implementation by avoiding conditioning of the model.[54,56]

Despite their superior performance, highly generative ML-based algorithms are prone to some fundamental challenges, such as hallucinations,[57,58] which are unphysical or incorrect predictions that drastically limit reliability in practical applications. This underscores the need for careful testing and evaluation to ensure these approaches can accurately reproduce the underlying physical behaviour of the systems being studied. In fact, since InDI learns the degradation process directly from the real data,[54] it reflects a more deterministic ansatz; therefore, it should also be less prone to hallucinations than standard diffusion models.

In this work, we present a generative AI-based workflow for enhancing 4D nano-SXCT images of miniaturized lithium-ion batteries comprising a silicon suboxide (SiO_x) anode, a separator and an NMC cathode. The custom-designed cells optimize X-ray transmission and spatial resolution, enabling *in situ* nano-tomography at the single-particle level with feature sizes on the order of several hundreds of nanometres. Unlike traditional SXCT workflows which struggle with trade-offs between contrast, resolution, beam damage and field-of-view, the presented approach leverages the generative artificial intelligence (genAI)-based InDI algorithm to achieve superior image quality while maintaining a large field-of-view. Notably, the model requires only a single pair of low-quality and high-quality scans for training, which can be obtained immediately after the *in situ* measurement, minimizing the risk of beam-induced artefacts during electrochemical charging. The InDI-enhanced images show significantly improved perceptual quality and a twofold increase in measured spatial resolution, enabling more accurate downstream image analyses such as semantic segmentation. This facilitates the extraction of physical descriptors and microstructural features, crucial for understanding degradation mechanisms and capacity fade in silicon anodes. By providing clearer and more detailed temporal information, our workflow supports the investigation of dynamic processes during battery operation and serves as a foundation for both physics-based and data-driven modelling approaches. Moreover, our results demonstrate that InDI minimizes the likelihood of introducing unphysical artefacts, making it especially well-suited for scientific applications where structural fidelity is essential. Furthermore, while this study focuses on lithium-ion battery materials, the presented workflow is not exclusive to this field and may have broad potential across various imaging-driven domains.

This journal is © The Royal Society of Chemistry 2025

J. Mater. Chem. A, 2025, **13**, 29930–29942 | **29931**

Results and discussion

Workflow of enhancing the image quality with the InDI model

For battery research, it is crucial to determine the key physical descriptors such as particle morphology and phase distribution, as well as temporal data on structural evolution over time. Semantic segmentation is one method for calculating these descriptors; however, achieving precise segmentation of particle features is challenging when working with datasets demonstrating insufficient resolution and contrast. As fine details may be obscured by a higher noise content, an effective resolution far below 1000 nm in nano-SXCT scans is usually necessary for both the electrode and Si-particles. To address this limitation, we employ an image enhancement strategy based on the implementation of generative AI. In particular, we implement an InDI algorithm in the image analysis workflow, which reduces noise, refines contrast and improves spatial resolution. This enables more reliable classification of microstructural features and subsequent calculation of important physical parameters. An overview of the main components in the proposed AI workflow, from experimental measurement to image-enhancement, is displayed in Fig. 1.

Fig. 1A schematically illustrates the *in situ* measurement setup at the ID16B beamline[59] of ESRF, employing X-ray holo-nano-tomography[60] suitable to trace the dynamic behaviour of the morphology during charging and discharging. The electrochemical cell has a cylindrical design measuring 1 mm in diameter, featuring a silicon-based anode, a polypropylene separator and a nickel–manganese–cobalt-oxide (NMC811) cathode. The cell is placed inside an *in situ* holder mounted on a rotating stage, allowing the X-rays to pass through in the direction perpendicular to the rotation axis. This configuration minimizes scattering artefacts from both the *in situ* cell holder and the copper current collector. The cell is connected to a potentiostat which is synchronized with the holo-tomography acquisition software,[61] enabling automated charging/discharging while performing tomographic scans at programmed time intervals; further details are provided in the Materials and methods section and Fig. S1.†

Fig. 1B illustrates the inherent dilemma between the voxel size and field-of-view (FOV) in nano-SXCT. High-quality (HQ) reconstructions, defined in this work as having $50 \times 50 \times 50$ nm^3 voxel size in x, y and z planes, respectively, enable fine structural detail but limit the imaged volume to a small FOV. In contrast, low-quality (LQ) scans, defined in this work to have $100 \times 100 \times 100$ nm^3 voxel size, allow for a larger FOV at the expense of image quality. In this specific case, the LQ images capture a volume of ∼200 μm^3, which is $8\times$ larger than the FOV of the HQ scan. Additionally, the HQ scan increases photon density compared to the LQ one, posing additional problems to beam sensitive materials.

In Fig. 1C, the measurement and training strategy including validation as well as the application of the image enhancement algorithm on an unseen data set is illustrated. Initially, a single pair of LQ and HQ nano-tomography measurements of a battery cell is obtained. These two initial scans are used to train the InDI model in a supervised manner to enhance the quality of the LQ images to match the HQ ones. Noticeably, the measurement for the initial training is performed only once.

After supervised training of the InDI model with the initial HQ and LQ measurements, InDI can be applied to enhance images of different battery cells which the model has never seen before. To show this, we perform *in situ* nano-tomography measurements on a second but identical cell. However, this time, only the LQ scans are taken, reducing beam damage and capturing a higher FOV than the HQ scans do. Furthermore, these second measurements are done in three key time steps during electrochemical loading to show the chemical evolution of the cell. Importantly, the model is not retrained for this second dataset, since no HQ scans are available. Further details are provided in the Materials and methods section.

Fig. 1D presents an LQ 3D rendering of a selected volume of interest within the anode, and the same image with InDI applied. Dark grey regions correspond to SiO$_x$ particles embedded in a lighter grey matrix, which includes binder, electrolyte and material below the resolution limit. We note that the purpose of InDI enhancement is to combine a wide FOV with high image quality, especially focusing on resolving the particles.

In Fig. 1D, we display the workflow of enhancing the X-ray nano-tomography images using the generative InDI approach. First, we slice the 3D data into 2D images (*xy*-planes) and enhance each slice individually – significantly improving contrast. To ensure isotropic voxel sizes in all three dimensions, we apply bicubic interpolation of the enhanced grey values along the axial direction. While direct 3D enhancement algorithms exist,[62–64] they usually require substantial computational resources, making them unfeasible for most research workflows. However, when changes between slices are small, a simple bicubic interpolation delivers equivalent results, see Fig. S2† for more information.

Our model architecture, depicted in Fig. 1D, follows a U-Net like structure with down-sampling and up-sampling blocks combined with skip connections. Because the InDI algorithm requires input and output images to have identical sizes, we first upscale the LQ scans using bicubic interpolation before the initial iteration. After the first iteration, the resulting enhanced image serves as the input for the next iteration, and this process continues until the desired quality is achieved or image quality degradation begins. Further details on the model architecture are provided in the Materials and methods section.

Training and testing of the InDI model for SXCT image data

As shown in Fig. 2A and B, we utilize the initial pair of LQ and HQ image data with $100 \times 100 \times 100$ nm^3 and $50 \times 50 \times 50$ nm^3 voxel sizes, respectively, to train and test the InDI algorithm. Hence, the HQ image has an eight times smaller FOV compared to the LQ image. Since we train the model in a fully supervised manner using paired images with different voxel sizes, we have to match the image volumes. To do this, we first crop and then upscale the LQ images by a factor of two,

29932 | *J. Mater. Chem. A*, 2025, **13**, 29930–29942

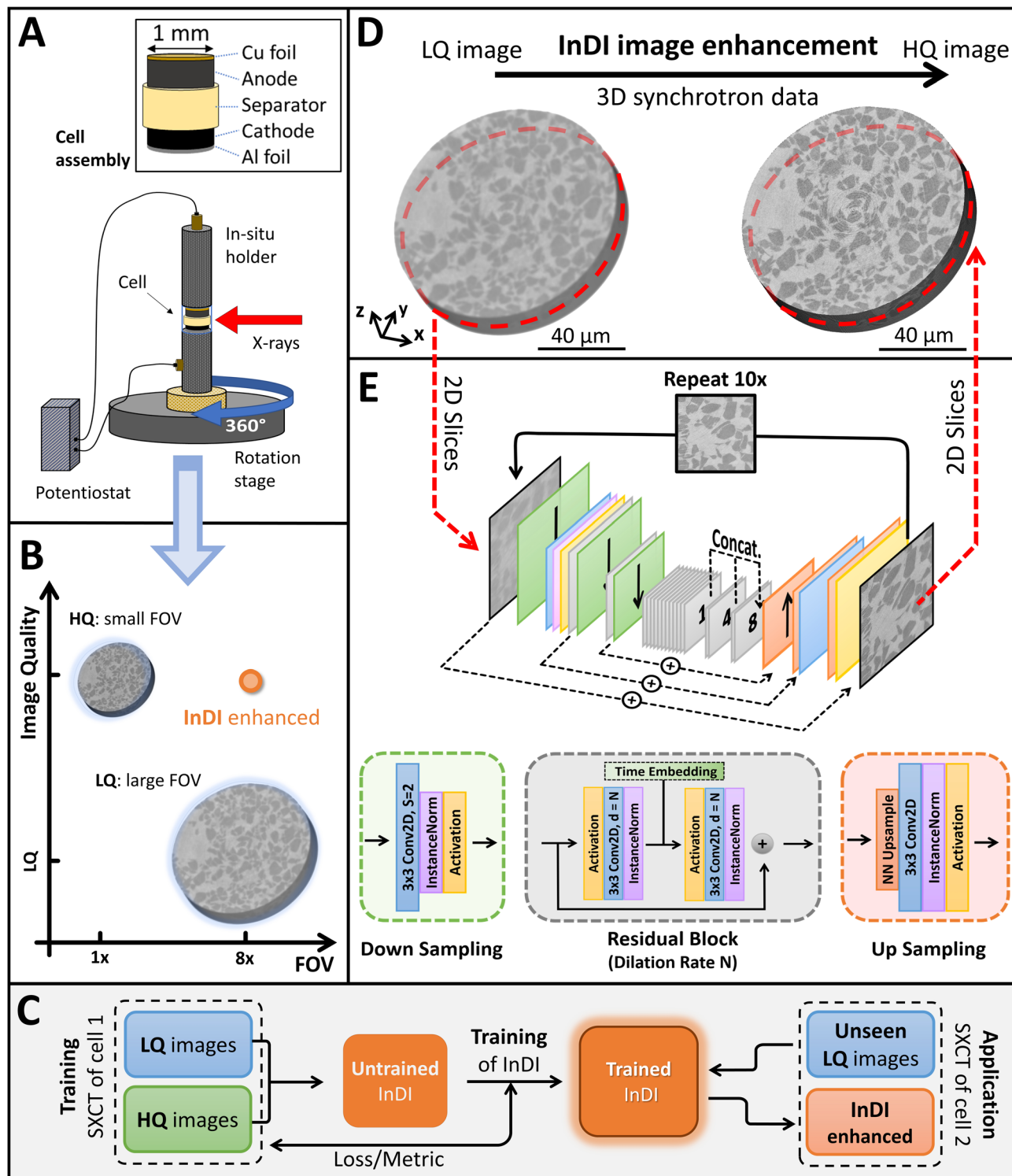This journal is © The Royal Society of Chemistry 2025

Fig. 1 Overview of the SXCT measurement workflow and InDI model architecture. (A) Schematic of the investigated LIB, featuring a Si-based anode coated on a thin copper foil, a separator, and an NMC cathode coated on a thin sheet of aluminium (not to scale). Below, the *in situ* holder setup at ID16B is illustrated. (B) Measurement strategy showing two voxel sizes: $100 \times 100 \times 100$ nm^3 voxel size (denoted as LQ), which captures a large field-of-view (FOV) but with lower image quality, and $50 \times 50 \times 50$ nm^3 voxel size (denoted as HQ), which offers enhanced image quality at the cost of reduced FOV. (C) Training and evaluation workflow. First, InDI is trained on acquired HQ and LQ data, then the trained InDI model is applied to unseen images. InDI enhancement aims to combine high image quality while maintaining a large FOV. (D) Example of a rendered sub-volume inside a reconstructed LQ 3D tomography image shown before and after InDI enhancement. A 2D cross-sectional slice (*xy*-plane) is highlighted with a red dashed circle. (E) U-Net-like model architecture with skip connections and dilated convolutions in the bottleneck layer. All kernel sizes are set to 3 except for the first and last convolutional layers in the network, where it is 7. The number of filters is set to 64 in the first layer and doubled after every down-sampling block. The last up-sampling layer before the final hyperbolic tangent (tanh) activation is a sub-pixel convolution.
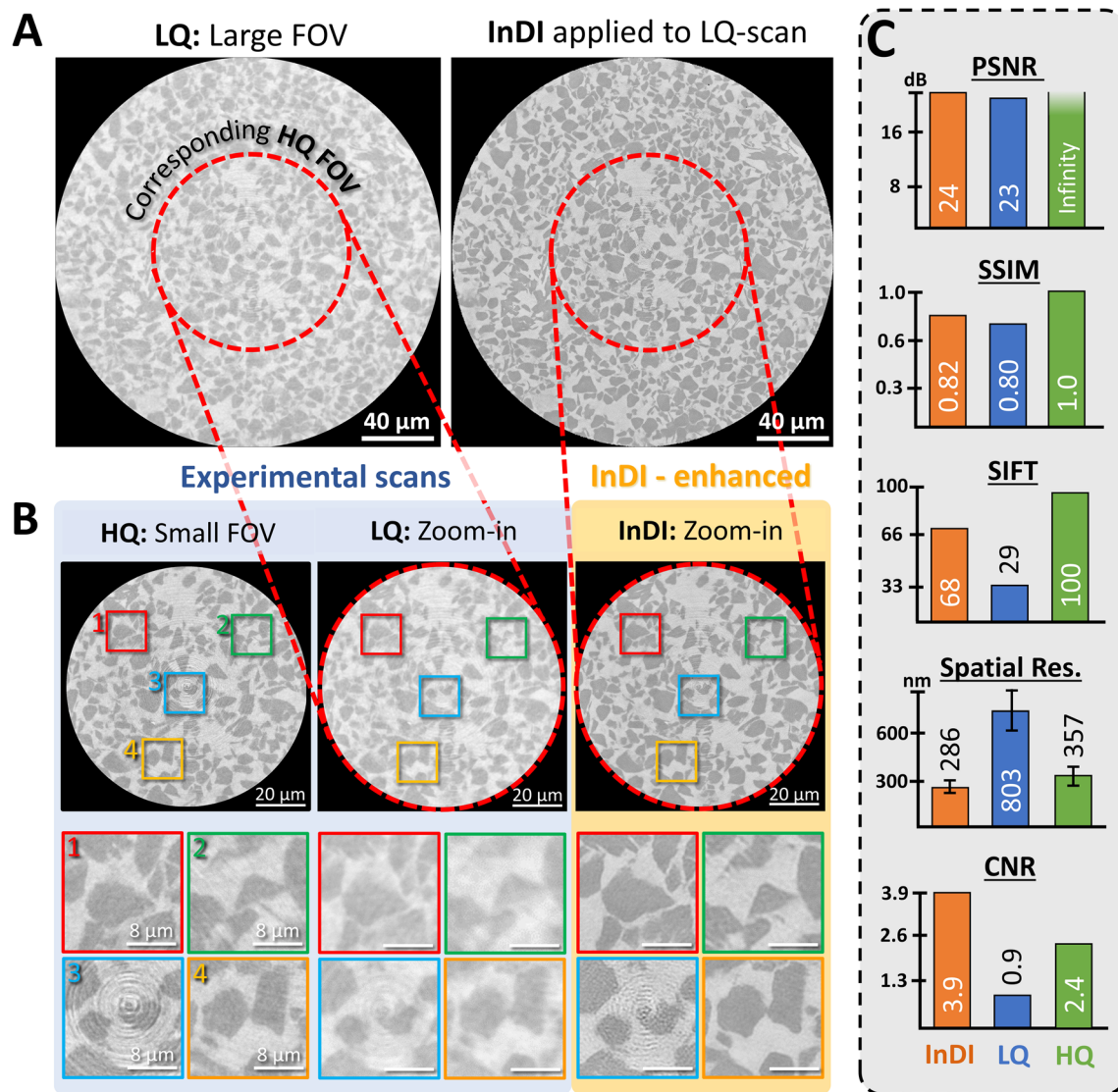
This journal is © The Royal Society of Chemistry 2025

J. Mater. Chem. A, 2025, 13, 29930–29942 | 29933

Fig. 2 Model evaluation and comparison on the test dataset. (A) SXCT *xy*-slice images with a large FOV. The left image is acquired at $100 \times 100 \times 100$ nm³ voxel size (LQ) in *x*, *y* and *z*, respectively, while the right image is the same slice enhanced using the InDI model. Red circles indicate the FOV captured by the $50 \times 50 \times 50$ nm³ (HQ) scan. (B) Comparison LQ, HQ and LQ after InDI enhancement. All images are cropped to the same FOV for direct comparison. Detailed zoomed-in views of specific regions of interest (ROI 1–4) are shown in coloured boxes. (C) Quantitative evaluation of InDI performance using four metrics: Peak Signal-to-Noise Ratio (PSNR), Structural Similarity Index (SSIM), SIFT-based feature matching, spatial resolution in nm and contrast-to-noise ratio (CNR). Higher values of PSNR, SSIM, SIFT and CNR indicate improved image quality relative to the HQ reference scan. Lower spatial resolution values correspond to an increased ability to distinguish finer structural details from the background.

obtaining the same imaged volume as the HQ images. However, acquiring a holo-tomography scan at different voxel sizes requires translating the sample along the X-ray beam axis from closer to further away to the focal spot, Unavoidably leading to slight misalignments among the cropped and upscaled reconstructed volumes. To address these misalignments, we utilize the spam.register image sub-pixel registration algorithm from the SPAM library.[65] Around 10% of the dataset is excluded from training and reserved for evaluation and testing. Further details on training and cropping are provided in the Materials and methods section.

Fig. 2A shows an exemplary LQ *xy*-slice used for testing, along with its InDI-enhanced version. During testing, we observed that image quality improves for about 7 to 10 iterations in the InDI procedure. Decreasing the number of iterations produces blurrier images due to the so-called regression-to-the-mean effect.[53] Contrarily, using a higher number of iterations leads to the amplification of unwanted noise or ring artefacts. Furthermore, the pixel-wise enhancements achieved by InDI cannot be solely accounted to a global contrast adjustments or histogram matching of the image.

Fig. 2B compares the HQ image with the LQ, as well as the InDI-enhanced image. A qualitative comparison between the experimental and generated images indicates that InDI improves both phase contrast and sharpness, revealing
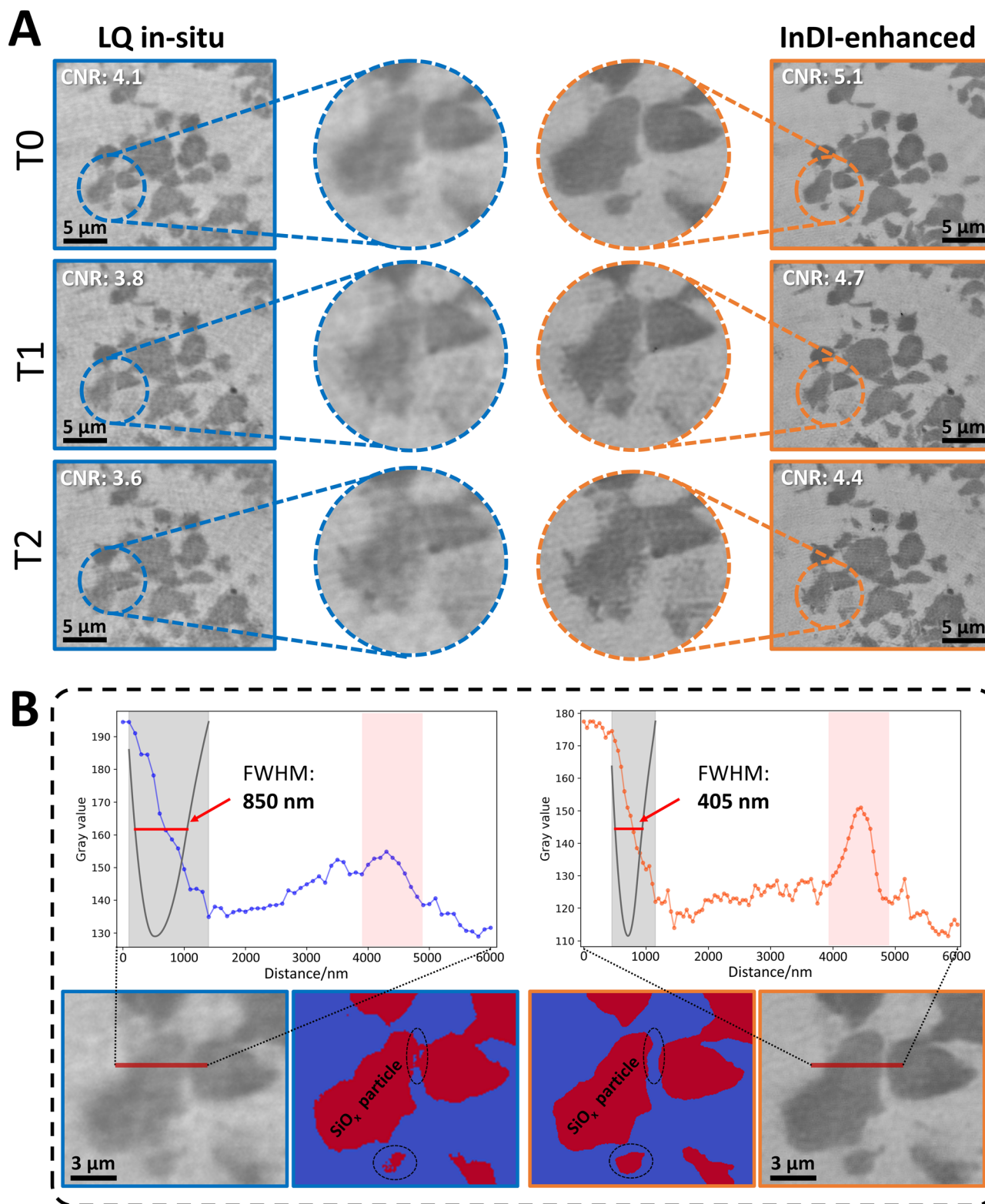
29934 | *J. Mater. Chem. A*, 2025, **13**, 29930–29942

This journal is © The Royal Society of Chemistry 2025

Fig. 3 *In situ* X-ray tomography measurements at different time steps. (A) Tomography *xy*-slice images of the same region at three timesteps: the uncharged state (T_0), an intermediate state (T_1) and the first fully charged state (T_2). Original LQ images (left, blue) are acquired at $100 \times 100 \times 100$ nm^3 voxel size in *x*, *y* and *z*, respectively, while InDI-enhanced reconstructions (right, orange) have $50 \times 50 \times 50$ nm^3 voxel size. Zoomed-in views of specific regions are presented in the middle for detailed comparison across all time steps. Contrast-to-noise ratio (CNR) values are calculated for all timesteps and indicated on the left. (B) Intensity profiles (grey values) along the red lines in the images. The intensity profile of the InDI-enhanced image (orange) shows deeper trenches and higher peaks compared to the original (blue), indicating sharper edges and improved contrast. This effect is qualitatively highlighted in the red-shaded area, which emphasizes enhanced particle separation in the InDI image. The intensity profile also includes an exemplary calculation of spatial resolution, where the black line represents the derivative of the intensity profile

This journal is © The Royal Society of Chemistry 2025

J. Mater. Chem. A, 2025, **13**, 29930–29942 | **29935**

previously indistinguishable details in the LQ image. This effect is particularly evident on small particles and particle edges.

Fig. 2C quantifies the improvements using different metrics. Since the low- and high-quality images are not perfect pixel-wise matches, classical metrics for quantifying the restoration quality, such as the Peak Signal-to-Noise Ratio (PSNR) or Structural Similarity Index (SSIM),[66] show close to no improvement due to InDI, even though quality has improved noticeably. These metrics heavily depend on pixel-level restorations, making them sensitive to even small pixel shifts, like translations or rotations, which can lead to inaccurate evaluations. To address this, we introduce two additional metrics that better capture physical image characteristics. The first is based on the Scale Invariant Feature Transform (SIFT) algorithm,[67] which identifies congruent features between images. A higher number of congruent features indicates better restoration quality. Notably, applying InDI more than doubles the number of congruent features compared to the original LQ image, demonstrating its effectiveness in restoring fine details. More information on our SIFT metric is provided in the Materials and methods section.

Furthermore, we assess the spatial resolution, to quantify how well the SiO_x particles within the anode can be distinguished from the background. Spatial resolution is defined as the full width at half-maximum (FWHM) between foreground particles and background pixels and has a unit of nm. Details can be found in Materials and methods as well as in Fig. S5.† In fact, the spatial resolution of the InDI-enhanced image (286 ± 25 nm) is comparable to that of the HQ image (357 ± 53 nm) and even surpasses it in some cases. The spatial resolution of the LQ image is 803 ± 135 nm and therefore significantly lower.

This slight superiority of InDI compared to the HQ image is likely due to a reduction in noise and artefacts. To test this argument, we evaluate the contrast-to-noise ratio (CNR) between foreground SiO_x particles and background in Fig. 2C. The extracted CNR is 3.9 and 2.4 for the InDI enhanced and HQ images, respectively. For the LQ image data, the CNR is significantly lower, measuring 0.9.

Finally, we compare the InDI with CNN- and GAN-based model architectures. See the ESI† for further information on the model structure. As illustrated in Fig. S3 and S4,† the CNN-based architecture clearly suffers from regression-to-the-mean, while the GAN exhibits training instability and overamplifies unwanted image artefacts. The analysis of the spatial resolution obtained for the CNN and GAN is 550 ± 54 nm and 392 ± 68 nm, respectively, which are significantly higher than that obtained for the InDI model. The ability of InDI to achieve a balance between detailed reconstructions and avoiding unwanted artefacts is the main advantage compared to CNN-based models and GANs. It is also obvious that InDI provides a major speedup compared to classical diffusion-based algorithms. Classical diffusion-based models usually require up to several thousands of iterations[55] for reconstruction.

Application of the InDI image enhancement algorithm to LQ *in situ* image data

After training and testing the model on the initial two measurements, it is applied to a different unseen LQ dataset acquired *in situ* during a second experiment. The LQ scan reduces beam damage and enables an increase of the FOV compared to a HQ scan. Note that no corresponding HQ data are acquired in this second measurement and that the model is not retrained – the pretrained model from the last section is used throughout this chapter.

Fig. 3A illustrates the microstructural time evolution of the Si-based anode captured by the *in situ* measurements. Three key time steps upon electrochemical charging (lithiation) are denoted as T_0, T_1, and T_2. T_0 represents the pristine, uncycled state. T_1 corresponds to an intermediate stage during the first charging cycle. T_2 denotes the fully charged state at the end of the first cycle. The left column shows original LQ *in situ* tomography slices, while the right column presents the corresponding enhanced images by applying the generative InDI model. To provide better visual insights, magnified regions of interest for all time steps are displayed in the middle column of Fig. 3A, emphasizing structural details and changes throughout the charging process. CNR values between background and SiO_x particles are calculated to quantify changes between timesteps and improvements due to InDI, see Table 1 and Fig. 3A. In fact, the InDI enhanced images show a higher CNR in all cases. Also note that the CNR values depicted in Table 1 are higher than the ones denoted in Fig. 2C. This is mainly due to the absence of ring artefacts in the depicted regions of interest in Fig. 3A.

For the uncharged initial state at T_0 of the *in situ* experiment, the SiO_x particles (dark grey) exhibit a relatively uniform grey level, indicative of the pristine state. As electrochemical charging progresses to the time-step of T_1, notable morphological changes emerge. In the fully charged state at T_2, the image reveals an increase of the particle size and the development of surface fractures, also accompanied by a decrease in CNR. Further distinct dark regions appear, likely indicating new dense phases formed during electrochemical charging.

Fig. 3B presents an exemplary intensity profile with an illustration of how to calculate spatial resolution, highlighting the enhanced image quality and sharper particle boundaries in the enhanced image. The InDI-enhanced image exhibits deeper trenches and more pronounced peaks, indicating sharper edges and enhanced contrast. Notably, the spatial resolution improves from 866 ± 183 nm in the original LQ image to 378 ± 81 nm in the InDI-enhanced *in situ* image when averaged over several particles. Exemplarily, a peak located at approximately 4500 nm, is only marginally visible in the original LQ image, while it stands out clearly in the InDI-enhanced image. Although this feature could be a consequence of hallucinations, we argue, as will be discussed in the Conclusion section, that the model has learned to capture the underlying physics and generate meaningful results. In fact, the spatial resolution

at the particle edge, and the red line marks the full width at half-maximum (FWHM). Additionally, segmentation results from two machine-learning models, trained on the LQ and InDI-enhanced images, are shown, demonstrating improved accuracy, particularly at particle edges.

29936 | *J. Mater. Chem. A*, 2025, **13**, 29930–29942

This journal is © The Royal Society of Chemistry 2025

Table 1 Contrast-to-noise-ratios (CNR) for timesteps T_0 to T_2 in the *in situ* measurement. The CNR values are higher for the InDI-enhanced images, indicating clearer images and particles which are more distinct from the background. Furthermore, the CNR decreases from T_0 to T_2 which is due to the morphological changes of Si particles during electrochemical loading

Time-steps	Contrast-to-noise-ratio (CNR)	
	LQ *in situ*	InDI-enhanced
T_0	4.1	5.1
T_1	3.8	4.7
T_2	3.6	4.4

achieved by InDI on image data from a different cell, never seen by the model during training, matches the resolution of the reference images used for training and validation, see Fig. 2. This also emphasises good generalizability of the model across similar image datasets.

As emphasized by the segmentation plot in Fig. 3B, the improvements achieved with InDI also enhance subsequent quantitative analyses, such as phase segmentation. The increased phase contrast and spatial resolution facilitate the training of machine learning-based segmentation models by making microstructural features more discernible, which might otherwise remain undetected in the original LQ data. This is particularly beneficial for automated, computer-based analysis workflows, where improved phase segmentation contributes to more reliable statistical assessments of key morphological metrics and interface characteristics, such as particle integrity, porosity, and phase connectivity. To illustrate this, we train two distinct machine learning-based segmentation models using a single image slice from both the LQ and InDI-enhanced datasets.

As shown in Fig. 3B, when HQ or InDI enhanced images are available, accurate segmentation can be achieved even with limited training data, significantly reducing the need for extensive manual labelling and computational effort.[68] By reducing the dependence on large training datasets while maintaining high segmentation accuracy, this method enables more efficient and scalable image analysis. More details on the segmentation algorithm can be found in the Materials and methods. Further segmentation results, including difference maps, are displayed in Fig. S6.†

Conclusion

In situ imaging is essential to understand the dynamic microstructure evolution within battery materials upon electrochemical loading, such as particle expansion, or phase changes. However, challenges arise in maintaining high contrast to enable subsequent image classification for accurate microstructure feature extraction while also preserving a wide field-of-view in *in situ* nano-tomography. Accurate extraction of physical descriptors, such as particle size, morphology and phase distribution, is critical for both physical and data-driven

modelling approaches, including generative prediction of microstructure evolution. Inaccuracies in classification can lead to error propagation in these models, ultimately compromising the predictive power and the development of optimized battery materials.

To address these challenges, we introduce a genAI-based image enhancement workflow utilizing the InDI algorithm. By applying InDI, we successfully enhance the contrast and spatial resolution of low-quality SXCT scans of silicon anodes across a temporal dataset, using only a single pair of low- and high-quality scans for model training. Generalization capabilities of the model are tested on a second unrelated *in situ* measurement utilizing another assembled cell, capturing the temporal behaviour of the lithiation process during electrochemical charging. The improvements achieved by the application of the InDI model in spatial resolution and contrast can facilitate the segmentation and analysis of particle morphology, cracking, porosity, and interphase development, which are key descriptors linked to the capacity fade and mechanical failure. These high-fidelity features serve as inputs for both physics-based degradation models and machine learning approaches, enhancing the accuracy of lifespan predictions. In this way, the enhanced data quality supports a more mechanistic and predictive understanding of aging in high-capacity anode materials by shedding light on the mechanical and electrochemical degradation mechanisms underlying capacity fade and lithiation properties.

For practical applications, we propose two primary strategies for obtaining suitable training data, each having its trade-offs in terms image acquisition time, beam-damage and generalization capabilities. In the single-sample approach, the high-quality scan is acquired either at the initial time step, before structural changes occur, or at the final time step, using the same sample as in the *in situ* experiment. In the identical-sample approach, which is used in this study, a separate but identical sample is scanned at higher voxel sizes, ensuring that the *in situ* experiment remains undisturbed. However, this assumes some microstructural similarity between the two samples. The single-sample approach offers direct correspondence between high- and low-voxel size datasets but risks introducing beam damage to the *in situ* sample. The identical-sample approach avoids beam damage but requires more time and resources and relies on structural similarity between the samples, which may not always hold. For cases involving significant microstructural evolution, such as large-volume expansion or severe particle degradation, an improved strategy would involve acquiring two high-quality scans – one at the beginning for the pristine state and another at the end of the experiment, *e.g.* for a state of charge (SoC) of 100%. Even though our model architecture has shown to handle these changes to some amount, additional measurements can increase the ability to generalize across varying stages of the battery cycling process. This could be achieved using the single-sample approach or by conducting a parallel *in situ* experiment on an identical sample with only two scans (at the beginning and end), minimizing overexposure of the actual *in situ* sample. Future studies could further explore this dual-scan strategy.

This journal is © The Royal Society of Chemistry 2025

J. Mater. Chem. A, 2025, **13**, 29930–29942 | **29937**

Despite the demonstrated efficiency and generalizability of our approach, certain limitations should be considered. The InDI model is case-specific and may require retraining when applied to datasets with significantly different microstructures, such as those from other electrode architectures or battery chemistries. These so-called out-of-domain errors can also be observed when training InDI on an underrepresented or too small subset of the whole cell. Fig. S4† exemplarily demonstrates the effects of training InDI on a non-representative fraction of the LQ image, only containing 1/64 of the total volume. As a result, the model's ability to generalize to a larger, more heterogeneous area, which contain brightness and contrast variations, is limited. Nevertheless, out-of-domain errors are not specific to the InDI algorithm. Such errors are also observed for CNN- and GAN-based image enhancement models.[62]

Another concern in using highly generative machine-learning approaches for image enhancement is hallucinations. For example, while the additional peak in the InDI-enhanced image of Fig. 3B demonstrates a visual improvement, it also emphasizes the generative nature of InDI and its potential for unphysical hallucinations. Although such artefacts are an unavoidable aspect of generative image enhancement, they do not necessarily pose problems. The InDI architecture appears to generate visually realistic structures, which align with physical expectation in the tested cases, as evidenced by Fig. 2, where no unphysical artefacts are observed. While the possibility of unwanted image alterations in the in situ data of Fig. 3 cannot be entirely ruled out due to the absence of a HQ ground truth, the enhancements appear realistic, and any unphysical augmentations, if present, are minimal and likely negligible. This assumption is also underscored by the fact that InDI, in contrast to standard diffusion models, directly learns the physical degradation process from the real data, reducing its potential for hallucination.

In summary, the advancements presented in this study have a large potential for enhancing battery research and offer promising opportunities for other scientific and industrial disciplines that rely on high-resolution imaging of dynamic processes. For battery research, monitoring the evolution of electrode microstructures at the sub-micron scale during electrochemical charging is essential to derive deeper insights into the lithiation of the particles as well as underlying aging mechanisms. As illustrated, four-dimensional (4D) synchrotron X-ray nano-tomography (SXCT) allows the perception of such dynamic processes. The utilization of generative artificial intelligence (genAI) facilitates solving the dilemma between resolution and field-of-view. The InDI algorithm allows not only a larger FOV but also higher spatial resolution and promotes subsequent image classification with higher accuracy as well as improved statistical analysis. Extracted microstructure features as well as classified volume data foster physics-based battery model parametrization. Furthermore, the approach reduces invasive beam exposure by excluding the need to focus on small volumes, which is highly advantageous for beam sensitive materials such as those utilized in the battery.

The integration of machine learning-driven enhancement techniques, like InDI, into the routine of in situ characterization workflows could substantially accelerate not only battery innovation but also progress in other fields such as biomedical imaging,[69] high-temperature electrochemistry[70] or semiconductor manufacturing.[71] These applications similarly demand high spatial resolution and wide field-of-view while minimizing sample perturbation. Altogether, this makes InDI a versatile and scalable tool for applications across a wide spectrum of image-driven field.

Materials and methods

Material preparation and cell assembly

The silicon-based anode was prepared using 89.3 wt% silicon suboxide (SiO_x) particles, 8 wt% lithium polyacrylate (LiPAA), 1 wt% sodium carboxymethyl cellulose (Na-CMC), 1.5 wt% carbon black and 0.2 wt% carbon nanotubes (CNTs). The electrode slurry was cast onto a battery-grade copper foil, resulting in electrodes with an areal capacity of 3.0 mA h cm^{-2}. As the cathode, nickel–manganese–cobalt oxide (NMC811, 3.0 mA h cm^{-2}) was employed. Circular electrodes with a diameter of 1.0 mm (corresponding to a geometric area of 0.8 mm^2 and a nominal capacity of ~25 µAh) were punched out and assembled in a layered configuration into an in situ electrochemical cell setup. The electrodes were separated by a non-woven polypropylene separator (1.5 mm diameter), soaked in 0.5 µL electrolyte comprising 1 M lithium hexafluorophosphate (LiPF$_6$) in fluoroethylene carbonate (FEC) and diethyl carbonate (DEC) (2 : 8 v/v) with 2 wt% vinylene carbonate (VC).

The in situ cell housing was constructed from a perfluoroalkoxy alkane tubing (inner diameter: 1.6 mm; outer diameter: 3.2 mm), which is transparent to X-rays and sealed with threaded steel mounts screwed into the polymer tubing. A spring contact within the upper steel mount was then adjusted to apply a specified external pressure (~0.5 MPa) on the cell. To prevent air penetration, the contact interface between the polymer and steel was further sealed with lacquer. Cell assembly was conducted entirely in an argon-filled glove box to maintain an inert environment.

In situ X-ray nano-tomography measurement

X-ray nano-tomography was performed at the ID16B beamline[59] of the European Synchrotron Radiation Facility (ESRF) in Grenoble, France, using holo-tomography.[60] A voxel size of $100 \times 100 \times 100$ nm^3 was used for in situ scans, while training data were generated by measuring a separate, identical sample at $100 \times 100 \times 100$ nm^3 and $50 \times 50 \times 50$ nm^3 voxel sizes, ensuring that the in situ experiment remains undisturbed. Holo-tomographic imaging involved phase-contrast acquisition at four sample-to-detector propagation distances, enabling accurate phase retrieval. The X-ray beam was monochromatic and conical, operating at an energy of 29.6 keV with a flux of 10^{12} photons per second. Each tomographic scan consisted of 2505 projections captured during a 360° sample rotation, with an exposure time of 20 ms per projection. Additionally, 20

29938 | *J. Mater. Chem. A*, 2025, **13**, 29930–29942

This journal is © The Royal Society of Chemistry 2025

reference and 21 dark-field images were recorded per scan. Data acquisition utilized a PCO edge 4.2 CMOS camera (2048 × 2048 pixels) with a 30 μm thick LSO scintillator. The total time per holo-tomography acquisition was approximately 10 minutes.

The *in situ* electrochemical cell was charged at a rate of C/3 using an OrigaFlex OGF500 potentiostat synchronized with the holo-tomography acquisition software.[61] In collaboration with ESRF, a workflow was developed to integrate electrochemical control with holo-tomography imaging, ensuring synchronized measurements through automated scripts that coordinate charging parameters and acquisition timing. Holo-tomography acquisitions were performed every 40 minutes during a single charging cycle. To reduce mechanical and thermal relaxation artefacts in the reconstructed images, the charging program was paused 1 minute before each acquisition, setting the cell to open-circuit potential (OCP). Once the holo-tomography acquisition was completed, charging resumed (see the ESI†).

Data reconstruction and processing

The 3D reconstruction process included an initial phase retrieval calculation, using a custom in-house octave script based on a Paganini-like approach, with a delta/beta ratio of 170. Filtered backprojection reconstruction was then performed using the ESRF software PyHST2.[72] Post-reconstruction ring artefact reduction was achieved using an in-house script. Final reconstructed volumes of $102.4 \times 102.4 \times 102.4 \ \mu m^3$ and $204.8 \times 204.8 \times 204.8 \ \mu m^3$, corresponding to voxel sizes of $50 \times 50 \times 50 \ nm^3$ and $100 \times 100 \times 100 \ nm^3$, respectively, were obtained in 16 bit unsigned integer format. To enhance the contrast of the images, we further postprocessed them by applying histogram equalization.

Postprocessing of reconstructed volumes for InDI

To prepare the training data for the InDI model, it is critical to ensure alignment between LQ and HQ reconstructed 3D images. Misalignments between reconstructed volumes at different voxel sizes in synchrotron X-ray tomography arise from factors such as variations in the source-to-detector distance (caused by changes in magnification) minor mechanical shifts during sample repositioning[73] and different image alignments of the four distance datasets during the phase retrieval calculation step. To address these misalignments, we utilized the spam.register image sub-pixel registration algorithm from the SPAM library.[65] The $100 \times 100 \times 100 \ nm^3$ voxel size training data were first upscaled by a factor of two (through a bicubic interpolation) to match the voxel size of the higher-quality data. A circular mask with a radius of 1024 pixels was applied to all slices in the x, y-plane to exclude image data in the peripheral region. Subsequently, non-rigid registration was performed to align the two 3D volumes. The computed transformation function from this calculation was applied to the LQ data, achieving the best possible alignment of the volumes in both horizontal and vertical planes. Even though this should ensure an optimal overlap of features across the two datasets, small deviation can still be observed. To ensure precise spatial alignment of the reconstructed volumes across different

time steps in the *in situ* scans, the spam.register image sub-pixel registration algorithm was applied.

Training details and model architecture

A total of 250 sliced and paired LQ and HQ images with a size of 2048 × 2048 px were used for training. 10% of these were reserved for validation and testing. Since the field-of-view (FOV) of the HQ image was eight times that of the LQ image, the peripheral regions of the LQ image were also used for qualitative testing purposes. For training, a one cycle schedule[74] with cosine decay was used and training ended after 1600 epochs. The maximum learning rate obtained was 0.0005. A batch size of two was used, and images were randomly cropped to 640 × 640 px. Data augmentation included random flipping and random rotations. All images were normalized to a pixel range from −1 to 1. To ensure that the input and output images have the same dimensions, the LQ images were upscaled by a factor of two. Two up-sampling methods were evaluated: the nearest-neighbour (NN) interpolation and bicubic interpolation. In fact, bicubic up-sampling produced more homogeneous outputs, likely due to overshoot errors that resulted in pixel values exceeding the valid range. These values were subsequently smoothed by the tanh activation in the final layer. When bicubic interpolation was used without tanh activation, the results turned out to be similar to those obtained using NN upscaling with tanh activation. The loss function utilized during InDI training was a combination of Mean Squared Error (MSE) and Mean Absolute Error (MAE), similar to Huber loss. For the range 0 to 0.5, MAE loss was used, while MSE loss was used for larger values. This guaranteed that the gradient remained as large as possible for small and large values of the loss function.

We employed a U-Net-like[75] model architecture with skip connections and dilated convolutions in the bottleneck layer. Throughout the model, we applied Swish activation to the dying neuron problem, except in the final layer, where a tanh activation function was applied. Instead of using multiple down-sampling blocks, as is common in U-Nets, our model employed a combination of non-dilated and dilated convolutions in the bottleneck layer. This enabled us to capture both fine and coarse features. The last up-sampling layer in our architecture was set to a sub-pixel convolution to retain fine details. All convolutional kernels were 3 × 3, except for the first and last layers, which used 7 × 7 kernels. As is typical in U-Nets, we started with a small number of convolutional filters, 64 in our case, in the first block and doubled the number of filters after every down-sampling block. Time embedding was implemented through a sin/cos positional embedding of the time-step. This embedding was transformed by a dense layer and added to the convolutional input in the residual layer. All training and pre-processing were done on python TensorFlow 2.10 (ref. 76) on a NVIDIA RTX A5000 GPU with 24 Gb V-RAM and Intel Xeon w5-3433 CPU with 512 Gb RAM.

Using SIFT for quantifying image enhancement

To evaluate model performance, we employed a metric based on the Scale-Invariant Feature Transform (SIFT) algorithm.[67] SIFT

is a method that identifies important key points in an image in nearly scale-, rotation- and translation-invariant way. These key points are represented by high-dimensional and unique feature vectors. After identifying a set number of key points in both InDI enhanced and high-quality image, these points were then matched by calculating the Euclidean distance metric between the feature vectors. We call these matched features congruent points. The quality of the image enhancement was assessed based on the number of congruent points between the two images: a higher number of congruent points indicates a better enhancement, while a lower number suggests a lower image quality. The advantage of this method is its robustness to transformations, which negatively impacts traditional image quality metrics such as the Peak Signal-to-Noise Ratio (PSNR) and Structural Similarity Index (SSIM).

Calculating the spatial resolution and CNR

Spatial resolution was determined by manually identifying particle edges and analysing orthogonal line profile plots, as shown in Fig. 3B. At particle interfaces, grayscale values change due to phase transitions. The spatial resolution was calculated as the full width at half-maximum (FWHM) of the derivative of the grayscale values at the interface, which was approximately described by a quadratic function. More details and example plots can be found in Fig. S5.†

For calculating CNR values, semantic segmentation of particles and background was carried out. The particles were considered as foreground pixels which have to be distinguished from the background, and CNR was calculated between these two domains. Note that CNR is noticeably affected by ring artefacts, noise and also particle growth during electrochemical loading.

Machine-learning image segmentation

To segment different material phases in tomography volumes, a convolutional neural network (CNN)-based approach was implemented using an attention residual U-Net model[68] and the Python Keras library. Two models were trained: one on a 1024 × 1024 px InDI-enhanced image and another on the same image at its original LQ voxel size (512 × 512 pixels), along with their respective labels. Initial labels were generated using the open-source software Ilastik. The images were divided into four sub-images and augmented three times to expand the training dataset. The CNN models were trained on 16 images of 512 × 512 px (InDI-enhanced) and 256 × 256 px LQ, respectively, for 150 epochs using an NVIDIA RTX A5000 GPU. For additional details, see the ESI.†

Data availability

All data needed to evaluate the conclusions in the paper are presented in the paper. The InDI algorithm used for the analysis is publicly available at '**https://github.com/Nikolai10/Diffusion-TF**' (developed by Nikolai Körber). All other materials, including model architecture and pre-processing steps, are described in detail in the paper. Additional information can be obtained from the corresponding author upon reasonable request.

Author contributions

Conceptualization: M. H., R. W., and R. B.; experimental concept: M. H. and R. B.; material fabrication: C. S. and S. K.; sample preparation: M. H.; *in situ* measurement: M. H., R. J. S., O. S., J. V., and R. B.; development of the ML model: R. W.; model evaluation: M. H. and R. W.; visualization: M. H. and R. W.; supervision: R. B.; writing: M. H., R. W., and R. B.

Conflicts of interest

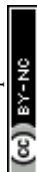The authors declare no conflicts of interest.

Acknowledgements

References

1 X. Wu, G. Ji, J. Wang, G. Zhou and Z. Liang, *Adv. Mater.*, 2023, **35**, 2301540.

2 G. G. Njema, R. B. O. Ouma and J. K. Kibet, *J. Renewable Energy*, 2024, **2024**, 2329261.

3 C. D. Quilty, D. Wu, W. Li, D. C. Bock, L. Wang, L. M. Housel, A. Abraham, K. J. Takeuchi, A. C. Marschilok and E. S. Takeuchi, *Chem. Rev.*, 2023, **123**, 1327–1363.

4 M. Fichtner, K. Edström, E. Ayerbe, M. Berecibar, A. Bhowmik, I. E. Castelli, S. Clark, R. Dominko, M. Erakca, A. A. Franco, A. Grimaud, B. Horstmann, A. Latz, H. Lorrmann, M. Meeus, R. Narayan, F. Pammer, J. Ruhland, H. Stein, T. Vegge and M. Weil, *Adv. Energy Mater.*, 2022, **12**, 2102904.

5 M. N. Obrovac and V. L. Chevrier, *Chem. Rev.*, 2014, **114**, 11444–11502.

6 Z. Zhang, Y. Wu, Z. Mo, X. Lei, X. Xie, X. Xue, H. Qin and H. Jiang, *RSC Adv.*, 2025, **15**, 10731–10753.

7 H. Seo, D. Kim, S. Park, E. Seo, P. Kim, J. Choi and J. Yoo, *Adv. Ind. Eng. Chem.*, 2025, **1**, 3.

8 J.-Y. Seo, S. Kim, J.-H. Kim, Y.-H. Lee, J.-Y. Shin, S. Jeong, D.-W. Sung, Y. M. Lee and S.-Y. Lee, *Nat. Commun.*, 2024, **15**, 10134.

29940 | *J. Mater. Chem. A*, 2025, **13**, 29930–29942

This journal is © The Royal Society of Chemistry 2025

9 M. T. McDowell, S. W. Lee, W. D. Nix and Y. Cui, *Adv. Mater.*, 2013, **25**, 4966–4985.

10 Y. He, L. Jiang, T. Chen, Y. Xu, H. Jia, R. Yi, D. Xue, M. Song, A. Genc, C. Bouchet-Marquis, L. Pullan, T. Tessner, J. Yoo, X. Li, J.-G. Zhang, S. Zhang and C. Wang, *Nat. Nanotechnol.*, 2021, **16**, 1113–1120.

11 Y.-X. Yao, L. Xu, C. Yan and Q. Zhang, *EES Batter.*, 2025, **1**, 9–22.

12 J. Zhao, F. Cai, B. Wang, J. Ren, Z. Guo, Y. Du, M. H. Helal, Z. M. El-Bahy, Z. Wang and J. Sha, *Adv. Colloid Interface Sci.*, 2025, **343**, 103543.

13 H. You, X. Wang, J. Zhu, B. Jiang, G. Han, X. Wei and H. Dai, *Energy Storage Mater.*, 2024, **65**, 103083.

14 T. Vorauer, P. Kumar, C. L. Berhaut, F. F. Chamasemani, P. H. Jouneau, D. Aradilla, S. Tardif, S. Pouget, B. Fuchsbichler, L. Helfen, S. Atalay, W. D. Widanage, S. Koller, S. Lyonnard and R. Brunner, *Commun. Chem.*, 2020, **3**, DOI: 10.1038/s42004-020-00386-x.

15 D. Schäfer, K. Hankins, M. Allion, U. Krewer, F. Karcher, L. Derr, R. Schuster, J. Maibach, S. Mück, D. Kramer, R. Mönig, F. Jeschull, S. Daboss, T. Philipp, G. Neusser, J. Romer, K. Palanisamy, C. Kranz, F. Buchner, R. J. Behm, A. Ahmadian, C. Kübel, I. Mohammad, A. Samoson, R. Witter, B. Smarsly and M. Rohnke, *Adv. Energy Mater.*, 2024, **14**, 2302830.

16 Z. Deng, X. Lin, Z. Huang, J. Meng, Y. Zhong, G. Ma, Y. Zhou, Y. Shen, H. Ding and Y. Huang, *Adv. Energy Mater.*, 2021, **11**, 2000806.

17 X. Zhang, M. Osenberg, R. F. Ziesche, Z. Yu, J. Kowal, K. Dong, Y. Lu and I. Manke, *ACS Energy Lett.*, 2025, **10**, 496–525.

18 B.-K. Cho, S.-Y. Jung, S.-J. Park, J.-H. Hyun and S.-H. Yu, *ACS Energy Lett.*, 2024, **9**, 4068–4092.

19 L. Zhao, M. Feng, C. Wu, L. Guo, Z. Chen, S. Risal, Q. Ai, J. Lou, Z. Fan, Y. Qi and Y. Yao, *Nat. Commun.*, 2025, **16**, 4283.

20 W. Li, Y. Liu, X. Yin, B. Wang and M. Zhang, *Optik*, 2015, **126**, 2788–2792.

21 C.-Y. Chen, T. Sano, T. Tsuda, K. Ui, Y. Oshima, M. Yamagata, M. Ishikawa, M. Haruta, T. Doi, M. Inaba and S. Kuwabata, *Sci. Rep.*, 2016, **6**, 36153.

22 M. Häusler, O. Stamati, C. Gammer, F. Moitzi, R. J. Sinojiya, J. Villanova, B. Sartory, D. Scheiber, J. Keckes, B. Fuchsbichler, S. Koller and R. Brunner, *Commun. Mater.*, 2024, **5**, 163.

23 V. Vanpeene, J. Villanova, J. P. Suuronen, A. King, A. Bonnin, J. Adrien, E. Maire and L. Roué, *Nano Energy*, 2020, **74**, 104848.

24 V. Vanpeene, J. Villanova, A. King, B. Lestriez, E. Maire and L. Roué, *Adv. Energy Mater.*, 2019, **9**, 1803947.

25 A. P. Black, A. Sorrentino, F. Fauth, I. Yousef, L. Simonelli, C. Frontera, A. Ponrouch, D. Tonti and M. R. Palacín, *Chem. Sci.*, 2023, **14**, 1641–1665.

26 Y. Liu, Q. Li and Z. Wang, *J. Energy Chem.*, 2024, **95**, 39–56.

27 C. E. L. Foss, M. K. Talkhoncheh, A. Ulvestad, H. F. Andersen, P. E. Vullum, N. P. Wagner, K. Friestad,

A. Y. Koposov, A. van Duin and J. P. Mæhlen, *J. Phys. Chem. Lett.*, 2025, **16**, 2238–2244.

28 S. Y. Lai, J. P. Mæhlen, T. J. Preston, M. O. Skare, M. U. Nagell, A. Ulvestad, D. Lemordant and A. Y. Koposov, *Nanoscale Adv.*, 2020, **2**, 5335–5342.

29 S. Haufe, R. Bernhard and J. Pfeiffer, *J. Electrochem. Soc.*, 2021, **168**, 080531.

30 W. An, B. Gao, S. Mei, B. Xiang, J. Fu, L. Wang, Q. Zhang, P. K. Chu and K. Huo, *Nat. Commun.*, 2019, **10**, 1447.

31 I. Dienwiebel, M. Winter and M. Börner, *J. Phys. Chem. C*, 2022, **126**, 11016–11025.

32 L. Gu, Y. Zhang, Q. Kong and C. Yang, *ChemElectroChem*, 2024, **11**, e202300602.

33 V. Vanpeene, L. Huet, J. Villanova, M. Olbinado, F. Marone, E. Maire, L. Roué, T. Devic and B. Lestriez, *Adv. Energy Mater.*, 2025, **15**, 2403741.

34 D. L. Nelson, S. E. Sandoval, J. Pyo, D. Bistri, T. A. Thomas, K. A. Cavallaro, J. A. Lewis, A. S. Iyer, P. Shevchenko, C. V Di Leo and M. T. McDowell, *ACS Energy Lett.*, 2024, **9**, 6085–6095.

35 D. P. Finegan, M. Scheel, J. B. Robinson, B. Tjaden, I. Hunt, T. J. Mason, J. Millichamp, M. Di Michiel, G. J. Offer, G. Hinds, D. J. L. Brett and P. R. Shearing, *Nat. Commun.*, 2015, **6**, 6924.

36 T. Jousseaume, J.-F. Colin, M. Chandesris, S. Lyonnard and S. Tardif, *ACS Energy Lett.*, 2023, **8**, 3323–3329.

37 S. A. Vaselabadi, D. Shakarisaz, P. Ruchhoeft, J. Strzalka and G. E. Stein, *J. Polym. Sci., Part B: Polym. Phys.*, 2016, **54**, 1074–1086.

38 A. P. Black, C. Escudero, F. Fauth, M. Fehse, G. Agostini, M. Reynaud, R. G. Houdeville, D. Chatzogiannakis, J. Orive, A. Ramo-Irurre, M. Casas-Cabanas and M. R. Palacin, *Chem. Mater.*, 2024, **36**, 5596–5610.

39 S. V Mohd Sagheer and S. N. George, *Biomed. Signal Process. Control*, 2020, **61**, 102036.

40 A. Kaur and G. Dong, *Neural Process. Lett.*, 2023, **55**, 7807–7850.

41 P. Liu, M. Wang, L. Wang and W. Han, *IEEE J. Sel. Top. Appl. Earth Obs. Remote Sens.*, 2019, **12**, 660–674.

42 J. Ma and F.-X. Le Dimet, *IEEE Trans. Geosci. Remote Sens.*, 2009, **47**, 792–802.

43 T. Plotz and S. Roth, in *Proceedings of the IEEE Conference on Computer Vision and Pattern Recognition (CVPR)*, 2017.

44 C. Ledig, L. Theis, F. Huszar, J. Caballero, A. Cunningham, A. Acosta, A. Aitken, A. Tejani, J. Totz, Z. Wang and W. Shi, *Photo-Realistic Single Image Super-Resolution Using a Generative Adversarial Network*, *arXiv*, 2017, preprint, arXiv:1609.04802, DOI: 10.48550/arXiv.1609.04802.

45 J. Yamanaka, S. Kuwashima and T. Kurita, in *Neural Information Processing*, ed. D. Liu, S. Xie, Y. Li, D. Zhao and E.-S. M. El-Alfy, Springer International Publishing, Cham, 2017, pp. 217–225.

46 X. Wang, K. Yu, S. Wu, J. Gu, Y. Liu, C. Dong, Y. Qiao and C. C. Loy, in *Computer Vision – ECCV 2018 Workshops*, ed. L. Leal-Taixé and S. Roth, Springer International Publishing, Cham, 2019, pp. 63–79.

This journal is © The Royal Society of Chemistry 2025

J. Mater. Chem. A, 2025, **13**, 29930–29942 | **29941**

47 C. Saharia, J. Ho, W. Chan, T. Salimans, D. J. Fleet and M. Norouzi, *arXiv*, 2021, preprint, arXiv:2104.07636, 10.48550/arXiv.2104.07636.

48 X. Li, Y. Ren, X. Jin, C. Lan, X. Wang, W. Zeng, X. Wang and Z. Chen, *arXiv*, 2023, preprint, arXiv.2308.09388, DOI: **10.48550/arXiv.2308.09388**.

49 M. Abdullah-Al-Wadud, M. H. Kabir, M. A. Akber Dewan and O. Chae, *IEEE Trans. Consum. Electron.*, 2007, **53**, 593–600.

50 P. Garg and T. Jain, *Int. J. New Technol. Res.*, 2017, **3**(9), 41–43.

51 R. A. Gopinath and C. S. Burrus, *IEEE Trans. Signal Process.*, 1994, **42**, 812–824.

52 M. Mafi, H. Martin, M. Cabrerizo, J. Andrian, A. Barreto and M. Adjouadi, *Signal Process.*, 2019, **157**, 236–260.

53 Y. Blau and T. Michaeli, in *2018 IEEE/CVF Conference on Computer Vision and Pattern Recognition*, IEEE, 2018, pp. 6228–6237.

54 M. Delbracio and P. Milanfar, *arXiv*, 2024, preprint, arXiv:2303.11435, DOI: **10.48550/arXiv.2303.11435**.

55 J. Ho, A. Jain and P. Abbeel, *arXiv*, 2020, preprint, arXiv:2006.11239, DOI: **10.48550/arXiv.2006.11239**.

56 Z. Zhan, D. Chen, J.-P. Mei, Z. Zhao, J. Chen, C. Chen, S. Lyu and C. Wang, *arXiv*, 2024, preprint, arXiv:2409.19365, DOI: **10.48550/arXiv.2409.19365**.

57 S. K. Aithal, P. Maini, Z. C. Lipton and J. Z. Kolter, *Thirty-Eighth Annu. Conf. Neural Inf. Process. Syst.*

58 Y. Sun, D. Sheng, Z. Zhou and Y. Wu, *Hum. Soc. Sci. Commun.*, 2024, **11**, 1278.

59 G. Martinez-Criado, J. Villanova, R. Tucoulou, D. Salomon, J.-P. Suuronen, S. Labouré, C. Guilloud, V. Valls, R. Barrett, E. Gagliardini, Y. Dabin, R. Baker, S. Bohic, C. Cohen and J. Morse, *J. Synchrotron Radiat.*, 2016, **23**, 344–352.

60 P. Cloetens, W. Ludwig, J. Baruchel, D. Van Dyck, J. Van Landuyt, J. P. Guigay and M. Schlenker, *Appl. Phys. Lett.*, 1999, **75**, 2912–2914.

61 V. Vanpeene, O. Stamati, C. Guilloud, R. Tucoulou, B. Holliger, M. Chandesris, S. Lyonnard and J. Villanova, *ACS Nano*, 2025, **19**(10), 9994–10012.

62 Y. Da Wang, Q. Meyer, K. Tang, J. E. McClure, R. T. White, S. T. Kelly, M. M. Crawford, F. Iacoviello, D. J. L. Brett, P. R. Shearing, P. Mostaghimi, C. Zhao and R. T. Armstrong, *Nat. Commun.*, 2023, **14**, 745.

63 Y. Wang, Q. Teng, X. He, J. Feng and T. Zhang, *Comput. Geosci.*, 2019, **133**, 104314.

64 L. Gambini, C. Gabbett, L. Doolan, L. Jones, J. N. Coleman, P. Gilligan and S. Sanvito, *Nat. Commun.*, 2024, **15**, 7962.

65 O. Stamati, E. Andò, E. Roubin, R. Cailletaud, M. Wiebicke, G. Pinzon, C. Couture, R. C. Hurley, R. Caulk, D. Caillerie, T. Matsushima, P. Bésuelle, F. Bertoni, T. Arnaud, A. O. Laborin, R. Rorato, Y. Sun, A. Tengattini, O. Okubadejo, J.-B. Colliat, M. Saadatfar, F. E. Garcia, C. Papazoglou, I. Vego, S. Brisard, J. Dijkstra and G. Birmpilis, *J. Open Source Softw.*, 2020, **5**, 2286.

66 D. R. I. M. Setiadi, *Multimed. Tools Appl.*, 2021, **80**, 8423–8444.

67 D. G. Lowe, *Int. J. Comput. Vis.*, 2004, **60**, 91–110.

68 F. F. Chamasemani, F. Lenzhofer and R. Brunner, *Sci. Rep.*, 2024, **14**, 21279.

69 L. Kong, M. Huang, L. Zhang and L. W. C. Chan, *Bioengineering*, 2024, **11**, 270.

70 H. Jiao, Z. Qu, S. Jiao, Y. Gao, S. Li, W.-L. Song, H. Chen, H. Zhu, R. Zhu and D. Fang, *Sci. Adv.*, 2022, **8**, eabm5678.

71 H. Villarraga-Gómez, K. Crosby, M. Terada and M. N. Rad, *J. Fail. Anal. Prev.*, 2024, **24**, 2113–2128.

72 A. Mirone, E. Brun, E. Gouillart, P. Tafforeau and J. Kieffer, *Nucl. Instrum. Methods Phys. Res., Sect. B*, 2014, **324**, 41–48.

73 C.-C. Cheng, C.-C. Chien, H.-H. Chen, Y. Hwu and Y.-T. Ching, *PLoS One*, 2014, **9**, 1–9.

74 L. N. Smith and N. Topin, *arXiv*, 2018, preprint, arXiv:1708.07120, DOI: **10.48550/arXiv.1708.07120**.

75 O. Ronneberger, P. Fischer and T. Brox, *arXiv*, 2016, preprint, arXiv:1505.04597, DOI: **10.48550/arXiv.1505.04597**.

76 M. Abadi, *et al.*, TensorFlow: A system for large-scale machine learning, *arXiv*, 2015, preprint, arXiv:1605.08695v2, DOI: **10.48550/arXiv.1605.08695**, **https://tensorflow.org/**.

77 M. Häusler, R. Sinojya, O. Stamati and R. Brunner, *Advanced Design Guidelines for Ceramic Based Solid State Energy Storage Systems [Dataset]*, European Synchrotron Radiation Facility, 2023, DOI: **10.15151/ESRF-ES-1033571027**.

78 M. Häusler, R. Sinojya, O. Stamati and R. Brunner, *Advanced Design Guidelines for Ceramic Based Solid State Energy Storage Systems [Dataset]*, European Synchrotron Radiation Facility, 2023, DOI: **10.15151/ESRF-ES-1190113340**.

29942 | *J. Mater. Chem. A*, 2025, **13**, 29930–29942

This journal is © The Royal Society of Chemistry 2025